The International Journal of Advanced Manufacturing Technology (2025) 137:2455–2470
https://doi.org/10.1007/s00170-025-15299-z

ORIGINAL ARTICLE

Generative network-assisted acceleration for microstructure simulation and prediction in laser-based additive manufacturing

Zhaochen Gu[1] · Aishwarya Manjunath[1] · Amrutha Anantatamukala[4] · Karri Venkata Mani Krishna[2,4] · Song Fu[1] · Shashank Sharma[2,3,4] · Narendra Bapurao Dahotre[2,3]

Received: 23 August 2024 / Accepted: 21 February 2025 / Published online: 4 March 2025

Abstract
In laser-based additive manufacturing, the process-structure–property paradigm has been critical for optimizing the fabrication of metallic components. The formation of anisotropic microstructures, primarily influenced by thermokinetics, has posed challenges in achieving desired mechanical properties. Computational methods such as cellular automata, phase field, and Monte Carlo simulations were traditionally employed to predict microstructural evolution; however, they have proven to be computationally intensive. This study employed a conditional generative adversarial network (GAN) utilizing the Pix2Pix architecture to predict microstructural evolution in laser-based additive manufacturing. The model was trained on over 1500 microstructure images generated by Kinetic Monte Carlo simulations with varying processing parameters, focusing on grain morphology and size distribution. Traditional image comparison metrics such as structural similarity index and mean squared error were deemed unsuitable due to their inability to capture higher-level features like grain structure. Instead, quantitative comparisons based on grain size distributions were employed to assess model performance. The results indicated strong efficacy in predicting equiaxed grain morphologies and accurately capturing grain size distributions, achieving the highest similarity score of $3.88e-2$ and the lowest distance score of 0.29. However, challenges were noted in predicting columnar grains, where larger grains were sometimes mispredicted as smaller. The findings suggested that a more balanced dataset could further improve performance, particularly in handling larger and columnar-shaped grains.

Keywords Surrogate modeling · Deep learning · Kinetic Monte Carlo · Microstructure prediction · Laser-based additive manufacturing

1 Introduction

In laser-based additive manufacturing (AM) of metallic components, understanding the process-structure–property (p-s-p) paradigm provides an optimization pathway toward fabricating components with the desired shape, size, and mechanical properties [1–3]. The grain morphology and size that evolve during alloy solidification in AM are predominantly influenced by several process-induced aspects like thermokinetics and local thermodynamics at the solidification front [4]. The layer-by-layer melting and solidification process establishes directional heat flow and a high thermal gradient along the build direction, leading to the formation of long columnar grains that span multiple build layers. This anisotropic grain structure is detrimental to the performance of AM components, as it can cause cracking and result in directional mechanical properties [1]. Naturally, the possible process pathways that lead to favorable thermokinetics for

✉ Narendra Bapurao Dahotre
Narendra.Dahotre@unt.edu

1 Department of Computer Science & Engineering, University of North Texas, 3940 N ELM Street, Denton, TX 76207, USA

2 Department of Material Science & Engineering, University of North Texas, 3940 N ELM Street, Denton, TX 76207, USA

3 Department of Mechanical Engineering, University of North Texas, 3940 N ELM Street, Denton, TX 76207, USA

4 Center for Agile and Adaptive Additive Manufacturing, University of North Texas, 3940 N ELM Street, Denton, TX 76207, USA

the formation of isotropic equiaxed microstructure have been explored extensively [5]. The transition from columnar to equiaxed grain structures has been reported to be influenced by thermo-kinetic parameters such as thermal gradient and solidification rate [4, 6]. High thermal gradients and slow solidification rates typically promote columnar grain growth, while lower temperature gradients and faster solidification rates favor the formation of equiaxed grains. For a given alloy composition, the processing conditions such as laser power, scan speed, layer thickness, melt pool size, and scanning strategy significantly affect the thermo-kinetic parameter variation vis-à-vis the resulting microstructure [2, 5].

Conducting trial and error-based experiments and microstructural characterization to optimize mechanical properties can be cumbersome, expensive, and time-consuming. Predictive modeling of thermo-kinetic-induced multi-layer and multi-track microstructure evolution offers a promising digital twin approach for p-s-p optimization. Various computational methods, such as cellular automata, phase field, lattice Boltzmann, and Monte Carlo methods, have been employed for such predictions [2, 5, 7, 8]. However, these methods require complex mathematical formulations and are computationally expensive in terms of run time. Consequently, machine learning-based surrogate modeling of these frameworks may provide a viable avenue for physics-informed digital twins, potentially offering a more efficient and cost-effective solution for optimizing the AM process [9].

Machine learning (ML) models have become foundational in various scientific, engineering, and domain-specific applications, assisting in improving processes and boosting productivity and quality through customized high-performance models for specific domains. A method called RCWGAN-GP, introduced by Tang et al. [10], utilized regression-based conditional generative adversarial networks with a Wasserstein loss function and gradient penalty to predict micrograph images based on a single parameter (laser power) for alumina microstructures during laser sintering. Additionally, ML and a 3D convolutional neural network (CNN) based on VGGNet were implemented to predict property-map microstructures and their corresponding mechanical properties, concluding that the deep learning model outperformed other ML methods in this task [11]. These studies explored the potential of microstructure prediction; however, the influence of various process parameters on microstructure formation was not considered. Recently, deep learning, particularly generative adversarial networks (GANs), was widely adopted in various applications in AM. In synthetic structure generation, several studies showed promising results [12–14]. Research also focused on enhancing image quality by improving resolution and clarity [15, 16], as well as using GAN networks for denoising to refine image analysis and grain segmentation [17–19]. Additionally, recent work explored generating mappings from microstructure to mechanical properties [20]. Anomaly detection in AM processes using GANs were also explored by Chung et al. [21]. Recently, GAN-based methods to model microstructure prediction considering laser power and surface emission brightness separately have also been reported [22]. Similarly, the generation of additional microstructure data to assist GAN-based microstructure modeling was proposed by Putz et al. [23]. In addition, recent studies have demonstrated the potential of cGANs in predicting critical features in additive manufacturing (AM) processes, such as the microstructural constituents of alpha and beta grains [24] and melt pool segmentation [25]. However, these approaches typically rely on limited datasets of experimental microstructural images, which are constrained by extensive characterization requirements and high costs. Such limitations pose significant challenges to developing broadly applicable cGAN models with strong generalizability. Although these works explored various applications using GAN networks, there remained a noticeable gap in addressing the mapping of various combinations of process parameters to microstructure. However, utilizing ML-assisted techniques for model training usually demands a considerable amount of data. Microstructural data, typically obtained through meticulous microscopy in experimental settings, constitutes a laborious and time-consuming process. The process of printing each sample involves gathering a substantial amount of powder, investing a significant amount of printing time, and performing highly cumbersome post-printing characterization. Due to the variability in parameters, accumulating sufficient data samples from experiments to meet the minimal requirements for model training may be prohibitively expensive in terms of time and costs. Therefore, to expedite the data generation process, a simulation-oriented method can be utilized to create microstructure images.

To that extent, a Kinetic Monte Carlo-based simulator developed by Sandia National Laboratories provides an elegant solution offering flexibility in printing multi-layer, multi-track AM blocks to generate microstructural data [26, 27]. The "potts" model facilitates the simulation of 3D microstructures by incorporating layer-by-layer solidification and grain evolution using the principal physical mechanisms of grain nucleation and growth. Moreover, the simulation framework enables the approximation of melt pool size and shape without material-specific parameters, offering considerable flexibility in generating different microstructure features. In addition, the provision of open-source code [28] renders this solution suitable for meeting current requirements of generating representative simulated microstructures as a function of AM influential parameters.

Following the above, in the present study, a conditional GAN-based image-to-image translation approach was employed, leveraging the Pix2Pix architecture [29] to learn

the mapping from input to output images. This approach is particularly suitable for transforming the input domain data (process parameters) into the output domain (microstructural images) due to the inherent feedback from the discriminator network to the generator network (defining characteristic of Pix2Pix framework). To the best of the authors' knowledge, this study demonstrated one of the first attempts, where a GAN-based approach was utilized to comprehensively predict microstructural evolution in laser-based AM. This approach shows significant promise in developing a GAN-based digital twin for microstructure prediction in laser-based additive manufacturing, providing a powerful tool for optimizing and understanding the complex relationships between process parameters and microstructural outcomes.

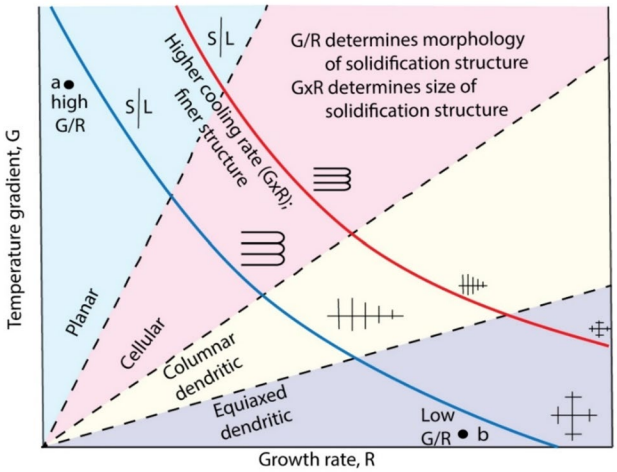

Fig. 1 Schematic illustrating solidification morphology with varying thermal gradient (G) and solidification rate (R) [1]

2 Methods

2.1 Microstructural data generation

The evolution of microstructure in laser-based AM depends on various process intrinsic factors that influence the solidification regime during the layer-by-layer printing process. Process parameters such as laser power, scan velocity, hatch spacing, and layer thickness profoundly affect the size of the melt pool and its shape, ultimately dictating the mode of solidification. Moreover, within a melt pool, specifically at the solidification front, the evolution of process-induced thermo-kinetic factors such as thermal gradient, solidification rate, cooling rate, and grain morphological factor affects the solidified grain morphology and grain size. In the AM process, as the solid–liquid interface progresses to solidify, local thermodynamics and kinetic can lead to transitions from a planar front to columnar dendritic or equiaxed dendritic structures [5, 30]. The literature has well established the causal relationship between thermo-kinetic variables and machine parameters [31–33]. Numerous experimental results document the formation of fully columnar, fully equiaxed, and mixed (columnar and equiaxed) grain morphologies in post-solidified AM components [2, 34–37]. Additionally, for a given set of process parameters, the spatial variation of thermo-kinetics within the melt pool, influenced by its curvature and shape, can lead to transitions in morphology from columnar to equiaxed within the AM component. Primarily, the post-solidification AM microstructure can be characterized by its morphology and size. Figure 1 illustrates the variation of grain morphology and its size with thermal gradient and solidification rate. Note that variations in machine parameters, including laser power, hatch spacing, layer thickness, and scanning speed, will significantly impact the thermal gradient. Additionally, changes in laser scanning speed will specifically affect the solidification rate. Thus, there exists a complex and intricate relationship between machine parameters and process thermokinetics, which is essential for developing a predictive framework for microstructure in AM.

In light of this, the process-microstructure modeling framework requires an accurate representation of process thermokinetics for reliable predictions. This necessitates a two-way coupling between the process model and the microstructure modeling framework. As discussed in previous section, the inclusion of all these elements in the mathematical modeling framework is cumbersome and computationally taxing. A Kinetic Monte Carlo (KMC)-based simulation framework developed by Sandia National Laboratories [26, 38] offers a pragmatic solution that provides flexibility by enabling the estimation of melt pool size and shape without the necessity of explicitly creating a mathematical process model. The synthetically generated idealized molten zone can provide track-by-track, layer-by-layer solidification history, which is further integrated with the underlying probabilistic Potts Monte Carlo algorithm to simulate the formation of solidified microstructures.

The KMC model is based on an on-lattice architecture, which relies on estimating grain evolution in AM by the curvature-driven grain growth within the thermal gradient developed in the HAZ of the molten pool. The parallelopiped structure of lattice sites defines the computation model; each lattice site is assigned an integer "spin," and neighboring lattice sites with the same spin constitute a grain. The local configurational energy at each lattice site is evaluated by comparing the spin at that site with the spins of its neighboring sites. Neighbors with opposite spins increase the system's total energy, whereas neighbors with identical spins do not affect the energy [26, 38]. The site energy E is calculated by the sum of all neighboring sites with different

grains. The number of neighbors (n) of the 3D microstructure simulation is 26.

$$E = \frac{1}{2}\sum_{i=1}^{N}\sum_{J=1}^{n} J_{ij}\left(1-\delta_{ij}\right),\ \delta_{ij} = \begin{cases} 0, \textit{for } i \neq j \\ 1, \textit{for } i = j \end{cases} \tag{1}$$

Equation 1 [39] shows the energy of a system E with a given microstructure [27] where N is the total number of sites, i and j represent single sites, and i is the index of each site ranging from 1 to the total number of sites (N), and j is the neighbor of site i ranging from 1 to the number of neighbors of sites n. The term J_{ij} is a constant that corresponds to the grain boundary energy. δ_{ij} is a Kronecker delta function. The grain evolution occurs by minimizing the system energy via the reassignment of lattice spin, as per the Metropolis algorithm described by the following equation:

$$P = \begin{cases} 1, & \Delta E < 0 \\ \exp\left(-\frac{\Delta E}{K_B T}\right), & \Delta E \geq 0 \end{cases} \tag{2}$$

where K_B is the Boltzmann constant, and T is the Monte Carlo temperature (does not correspond to the temperature evolution in AM [26, 38]). As described in Eq. 2, if the alteration in the spin of a lattice site results in a decrease in the energy of the system, the reassignment of the spin is accepted. Conversely, if the spin alteration resulted in an increase in system energy, the change could still be accepted if a random number was found to be less than P. The simulation duration was measured in Monte Carlo steps (MCS), with each MCS corresponding to the assessment of a lattice spin update at every site within the simulation domain.

In the current KMC framework, the microstructure evolution was confined to areas within and directly adjacent to the molten zone. This approach was justified since grain growth was unlikely in regions distant from the molten zone due to negligible grain boundary mobility [26, 38]. Although the heat source was not explicitly simulated, its impact was modeled by defining a molten zone bordered by a high-temperature heat-affected zone (HAZ) characterized by a steep thermal gradient. These combined zones created the conditions needed for microstructural changes. Figure 2 illustrates the idealized molten zone that could be prescribed in the KMC modeling architecture. The input parameters required to define such a melt pool were mainly melt pool width, melt pool depth, and HAZ width. Note that the units of these input parameters were defined by the number of lattice sites occupied by the idealized molten zone. The Metropolis algorithm was modified to accommodate grain boundary mobility, allowing the incorporation of solidification, grain evolution, and molten zone movement. The relationship between grain boundary mobility and temperature evolution within the HAZ region was described by the following equation.

$$P = \begin{cases} M(T), & \Delta E < 0 \\ \mathrm{M(T)}\exp\left(-\frac{\Delta E}{K_B T_s}\right), & \Delta E \geq 0 \end{cases};\ M(T) = M_o \exp\left(-\frac{Q}{RT}\right) \tag{3}$$

Note that in the above equation, T denotes the local temperature within the vicinity of HAZ, whereas T_s is the Monte Carlo calibration temperature. The grain growth in the HAZ is simulated by tuning the mobility $M(T)$ to be highest near the molten pool and $M(T) = 0$ far away from HAZ and the melt pool. In the presented case, the idealized molten zone, illustrated in Fig. 2, was rastered through the computational domain. The molten zone movement was based on a bi-directional laser scanning strategy with hatch spacing equal to half of the molten zone width. The overall dimension of the idealized melt zone was defined with respect to melt

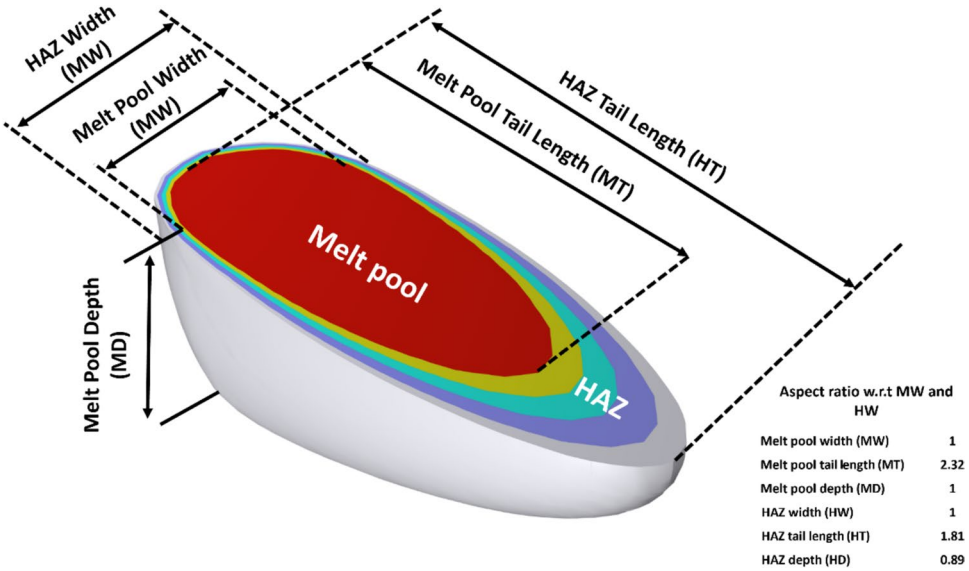

Fig. 2 Schematic illustrating 3D idealized molten zone and relevant dimensions used in the KMC framework to generate synthetic microstructure. (For interpretation of color in this figure, the reader is referred to the online version of the article)

width (MW) and HAZ width (HW) utilizing a pre-defined ratio, as illustrated in Fig. 2. The choice of the pre-defined ratio and idealized melt zone size was based upon preliminary simulation results runs. In addition, process parameters such as scanning speed, layer thickness, melt pool size, and heat-affected zone (HAZ) were varied to obtain a diverse set of microstructural features within the KMC framework. Table 1 enlists the magnitude and range of such variation in terms of KMC lattice sites. The selection of the specific combination of process parameters was based on the evaluation of kinetic strength, as recommended by [26, 38]. The values within the range are set up to facilitate a potential transition from columnar to equiaxed shapes.

Note that the SPPARKS framework employs a lattice-based distance unit rather than an absolute unit (viz m) for simulation. The simulation model utilizes a lattice, which is represented as a graph consisting of vertices and edges. Each vertex represents a lattice site located at a specific spatial position, with neighboring sites connected by graph edges. In the present case, a printed component was prescribed a size measuring $128 \times 128 \times 128$, containing a total of 2,097,152 lattice sites. Process parameter values are determined based on these lattice sites, with scanning speed representing the rate at which passes are made through the sites [39]. Note that the minimum values of the HAZ should be set larger than those of the melt pool and scanning speed to maintain logical consistency within the simulation.

In total, 1568 simulations were conducted to gather a diverse range of microstructure data, covering various grain structures, including columnar, equiaxed, and hybrid forms. These simulations will help understand trends and patterns within the data, ultimately assisting in the preparation of training data for the machine learning-based modeling of our research. The simulations were conducted on high-performance computers. Simulations were run on two nodes in parallel, each equipped with 128 cores. The CPU used is a $2\times$AMD EPYC 7763 64-core processor ("Milan") from the TACC Lonestar6 compute cluster [40]. Figure 3 illustrates some of the results obtained through 1568 simulation runs with process parameter variation. As can be observed, a diverse set of microstructures in terms of different grain morphologies and grain sizes was obtained. For instance, with an increase in the magnitude of scanning speed, the grain morphology shifts from long columnar grains to small equiaxed grains, and a similar morphological shift was obtained through the decrease in HAZ and melt pool width.

Table 1 Selected parameters with examined ranges and simulated values

Selected parameters	Range	Count
Melt pool width	[40, 10]	7
HAZ width	[91, 40]	7
Scanning speed	[3, 72]	8
Layer thickness	[11, 5]	4

2.2 Microstructure data curation

During the data curation phase, raw simulation files were systematically extracted and prepared for analysis. Files from the final dump of each simulation were retrieved to achieve a comprehensive overview of the simulated 3D blocks. Ovito [41], a scientific data visualization and analysis tool, was utilized to transform numerical data of KMC simulations into 3D visualizations, facilitating the observation of grain structure formation post-printing. Microstructural views across various layer distances and orientations were analyzed, highlighting potential variations resulting from physical influences during multi-layer printing. Consequently, the entire 3D-printed block was segmented into cross-sections to provide both horizontal and vertical perspectives of the internal structure.

As illustrated in Fig. 4a, grain structure images were obtained by sectioning perpendicular to the z-axis of the printed block to reveal top views of the grain structures at different layers. Similarly, multiple cross-sections were made along the y-axis to examine distinct grain patterns, such as columnar and equiaxed grains. Figure 4b depicts these cross-sections, offering a side view of the simulated samples across multiple layers in the xy plane, where columnar grain growth is evident. Considering the simulation box size was set to 128 lattice sites in each direction, cutting distances were specifically chosen at 32, 64, and 96 lattice sites. Moreover, areas exhibiting artifacts post-printing were assessed to identify un-melted regions and non-growing microstructures, which may arise due to the stochastic nature of the underlying algorithm. To ensure accurate insights into general grain structure development, consistency in the effective area of the simulated samples was maintained, facilitating precise observation of grain structure changes across multi-layer, multi-track printing simulations.

To discern the effect of process parameters on the different microstructure morphologies obtained using the Kinetic Monte Carlo (KMC) framework, each simulation data set was attached with a color-coded image representing various input parameters, such as scanning speed, melt pool width, heat-affected zone (HAZ) width, and layer thickness. The color coding was based on the normalization of the amplitude and range of variations of these respective input parameters. The normalized values were then color-coded using the jet colormap, with each color uniquely representing parameter values for machine learning training purposes. This integration allowed for a unique representation of the process conditions and the

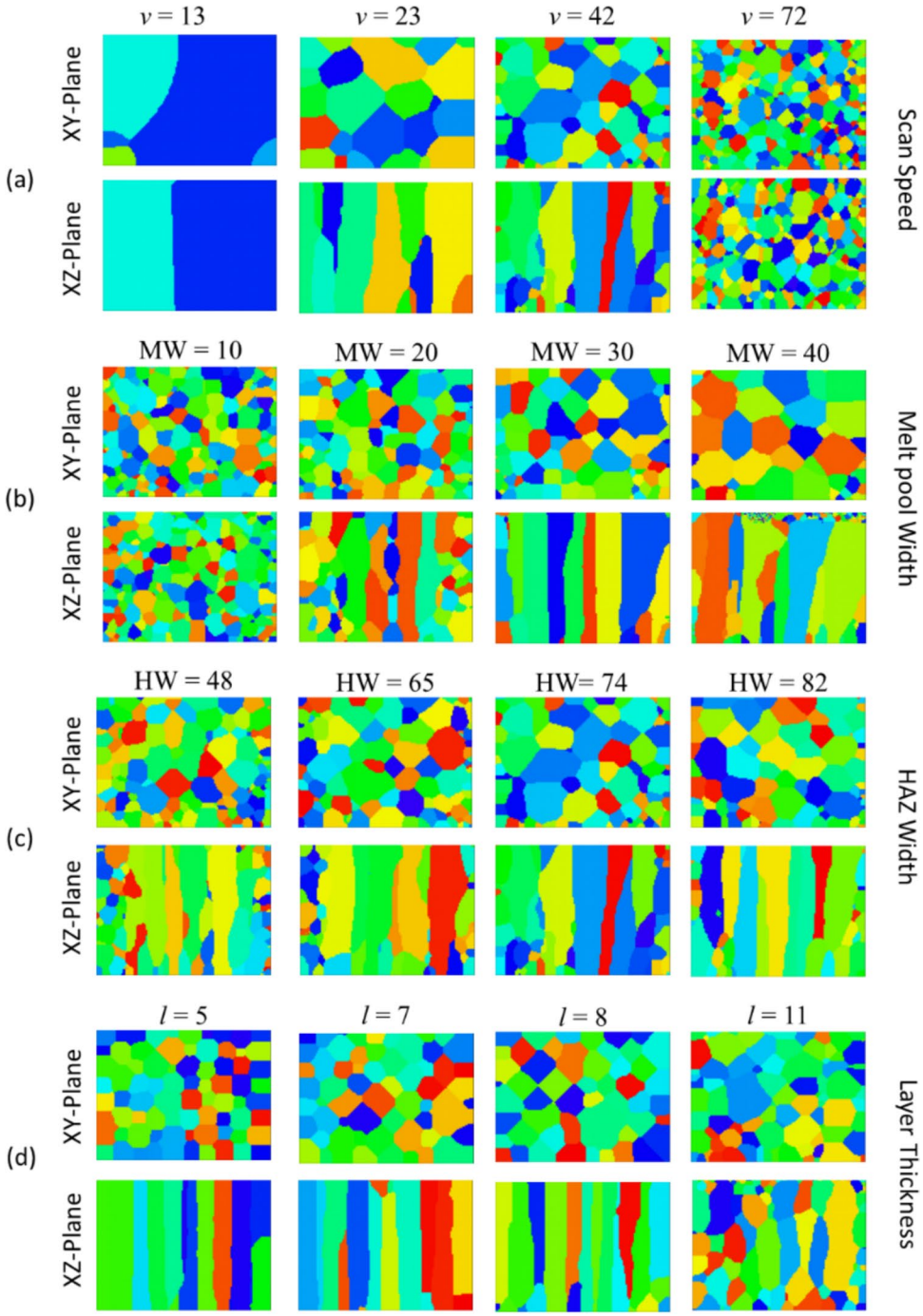

Fig. 3 Grain structure variation with process parameters: **a** scan speed (v) with fixed melt pool width of 25, HAZ width of 74, and layer thickness of 8. **b** Melt pool width (MW) with fixed scan speed of 42, HAZ width of 65, and layer thickness of 8. **c** HAZ width (HW) with a fixed scan speed of 42, melt pool width 25, and layer thickness of 8. **d** Layer thickness (l) with fixed scan speed of 13, melt pool width of 10, and HAZ width of 40

material microstructure. The input format of the KMC simulation dataset is illustrated in Fig. 5. This combined input for each simulation served as a training example for the subsequent GAN network of Pix2Pix. Subsequently, the data was partitioned into training and validation sets to facilitate model evaluation. Parameters with images were provided as input for training, and the expected output was a predicted grain structure image for each setting.

2.3 Microstructure modeling with machine learning

The proposed ML pipeline for microstructure prediction is illustrated in Fig. 6. For this task, a model based on a conditional generative adversarial network (GAN) has been chosen, utilizing the Pix2Pix network architecture [17, 29]. Pix2Pix was selected due to its capability to effectively translate input from one domain to another, making it particularly suitable for generating microstructure

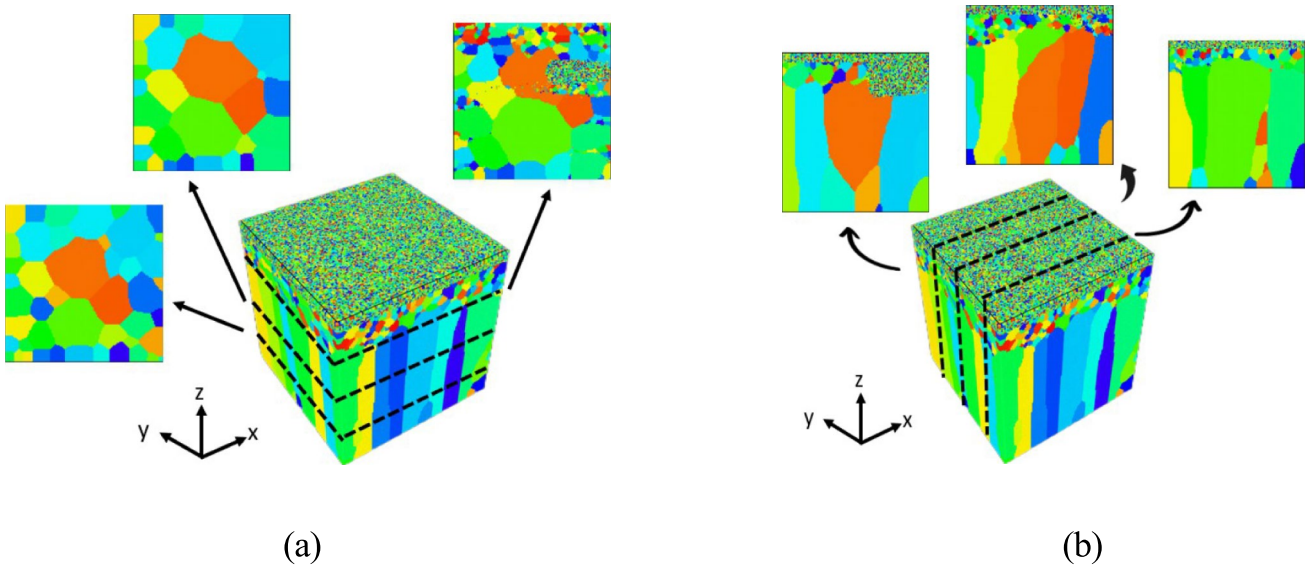

Fig. 4 Cross-sectional grain structure samples were collected from various directions and layer distances. **a** Sample retrieval from xy-plane (top view). **b** Sample retrieval from xz-plane (side view)

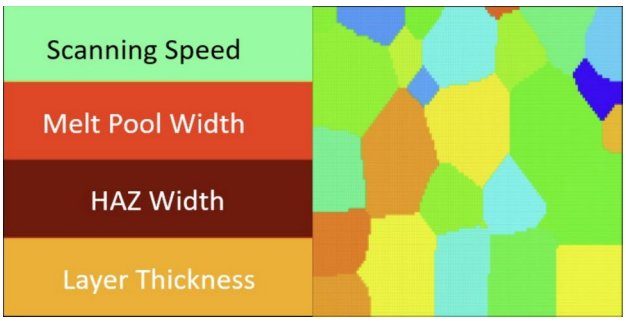

Fig. 5 Formatting the input training pair by combining the encoded process parameters and grain structure images (from KMC simulations) for machine learning training

images based on process parameters input with proper image representation.

GAN models are developed to create new data samples that resemble a given set of input microstructure images. This is achieved by using two neural networks, namely the Generator and the Discriminator, which are trained simultaneously in an adversarial manner. The Generator is responsible for generating new microstructure images, while the Discriminator assesses them against real images, thereby enhancing the model's capacity to deliver more realistic and accurate microstructural predictions. The input of the network consists of two parts: process parameter embeddings and target microstructure images. The selected process parameter values were encoded, initially in numerical format, into visual representations using corresponding pixel values and paired them with simulated microstructure images. These paired images were fed into the Generator, an encoder-decoder-based network, to generate synthetic microstructure images. The generated images, along with the simulated images, were then sent to the Discriminator. The Discriminator's task is to distinguish between real samples from the training data and "generated" samples produced by the Generator, using a binary classification mechanism. The Discriminator provides an output that is used to calculate the loss, which is subsequently used to further enhance and fine-tune both the Generator and Discriminator networks with backpropagation. The trained model was then applied to the testing dataset to predict the microstructure images based on different process parameter inputs.

2.4 Network training and model tuning

The generator network employs an encoder-decoder architecture. Specifically, the U-Net [42] is adopted. The Generator (G) takes random noises (z) and conditional inputs (y) (the encoded parameters) as inputs to generate a near-realistic microstructure image based on the condition. This can be expressed as

$$\hat{x} = G(y, z) \tag{4}$$

where $\hat{x}$ represents the generated microstructure image. The generator follows a U-Net architecture where the encoder first down-samples the input by applying convolution operations, with each layer block followed by batch normalization and ReLU activation functions. The convolutional operation

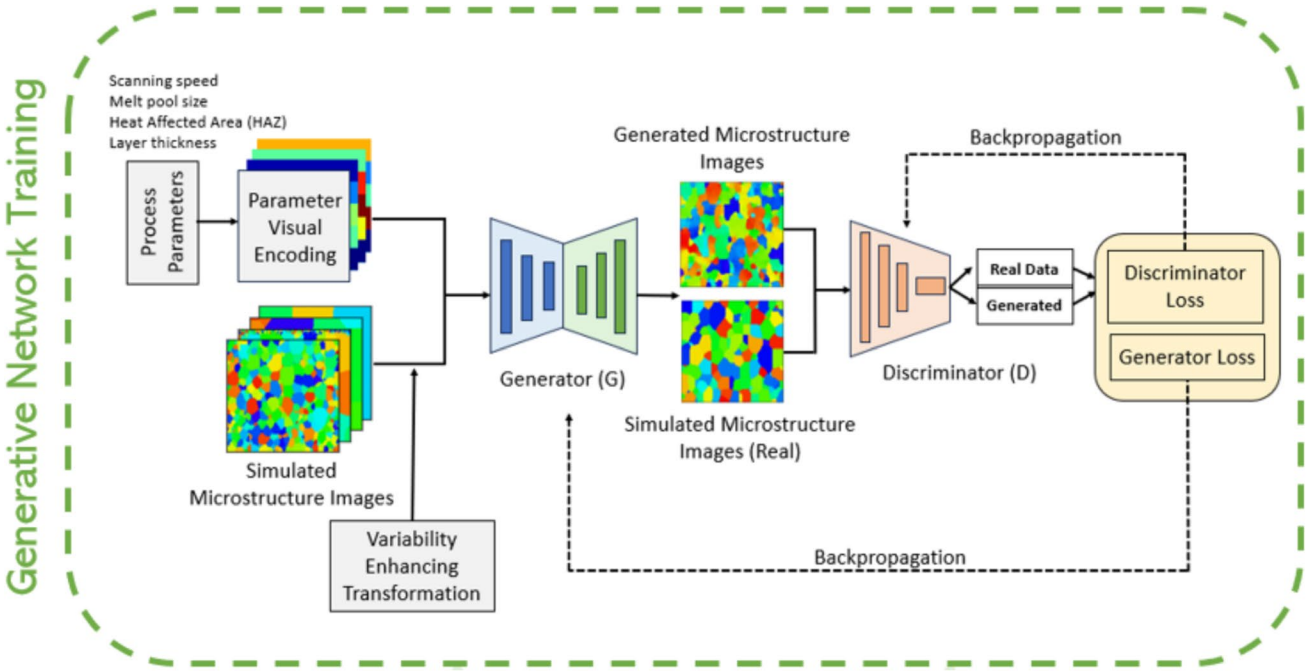

Fig. 6 Pipeline for simulation data acquisition and machine learning modeling

output feature maps ($x^{l}_{i,j}$) at each layer l computed as follows:

$$x^{l}_{i,j} = \sigma\left(\sum_{m,n} w^{l}_{m,n} \cdot x^{l-1}_{(i-m,j-n)} + b^{l}\right) \tag{5}$$

where $w^{l}_{m,n}$ represents the weight at position (m, n) in the convolution kernel at layer l. The $x^{l-1}_{(i-m,j-n)}$ denotes the corresponding pixel from the previous layer's feature map that aligns with the kernel. The summation applies the convolution operation across the entire input region.b^{l} is the bias term.

Batch normalization [43] is utilized to stabilize and accelerate the training process by normalizing the layer inputs to reduce the impact of "internal covariate shift" based on the varying distribution of each layer's inputs. The ReLU (Rectified Linear Unit) [44] activation function is chosen for its ability to introduce non-linearity into the network while preserving the benefits of sparse activation. ReLU also helps to reduce the risk of a vanishing gradient during training. Furthermore, the decoder part of the network then up-samples the feature maps by a factor of 2, using a spatial filter size of 4×4 and a stride value of 2, to effectively reconstruct the image from the compressed encoded representation. Additionally, the selection of the U-Net architecture benefits significantly from the integration of skip connections. These connections effectively convey low-level information between the corresponding input and output layers. This feature allows U-Net to outperform traditional encoder-decoder networks by preserving more detailed information across layers [29]. Moreover, the discriminator compares the real pair (y, x) with the generated pair $(y, G(y))$ and learns to classify whether the generated microstructure, $G(y)$, is closely resembles a real one. Specifically, it evaluates the similarity between the generated and real microstructure images and outputs a probability score. The process can be expressed as follows:

$$D(x, y) \rightarrow p_{real} \in [0, 1] \tag{6}$$

The fine-tuning process involves using the Adam optimizer [45] and Stochastic Gradient Descent [46] for both the generator and discriminator to achieve optimal performance. The Adam optimizer is preferred for its ability to enable fast convergence during training. It adaptively adjusts the learning rate for the model weights, allowing the model to use a higher learning rate when gradients are large and a lower one when they are small, which optimizes the learning process.

The loss function is critical to the model training and fine-tuning process. The loss function of the generator in this work is defined below. The loss function designed for the generator is comprised of three parts: conditional GAN loss, L1 loss, and L2 loss. The conditional GAN loss for the generator is defined as follows:

$$\mathcal{L}_{c\mathcal{GAN}}(G, D) = E_{y}\left[\log D\,(y)\right] + E_{x,z}\left[\log(1 - D(G(x, z)))\right] \tag{7}$$

The first part of the loss function calculates the expectation over real data samples by computing the probability that

the discriminator D correctly identifies real data as real. This is expressed through the log probability $\log D(y)$, where y represents real data points. The second part computes the probability that the discriminator D correctly identifies the generated data produced by the generator G as fake. It then calculates the expectation of this probability, represented by $\log(1 - D(G(x, z)))$. By combining these two components, the cGAN loss function enhances the adversarial training process, promoting mutual improvements in both the discriminator's ability to distinguish real from fake data and the generator's ability to create convincingly real data. Notably, the discriminator's loss only considers the first part of this function.

$$L_1(G) = \frac{1}{n}\sum_{i=1}^{n}\left|y_i - G(x,z)_i\right| \tag{8}$$

$$L_2(G) = \frac{1}{n}\sum_{i=1}^{n}\left(y_i - G(x,z)_i\right)^2 \tag{9}$$

As indicated in Eqs. (8) and (9), both the mean absolute error (L1 loss) and the mean squared error (L2 loss) are applied in our model. The L1 loss emphasizes model robustness and simplicity by minimizing the absolute differences between predicted and actual values, thus reducing the influence of less significant features by setting their coefficients to zero. On the other hand, the L2 loss is effective at handling outliers by minimizing their impact by squaring the error terms. Therefore, the model aims to combine these losses in the total loss equation to achieve optimal performance by leveraging the strengths of both approaches.

$$G^* = arg\ \min_G \max_D \mathcal{L}_{\text{cGAN}}(G,D) + \lambda_1 \cdot L_1(G) + \lambda_2 \cdot L_2(G) \tag{10}$$

Equation 10 represents the objective of finding the optimal generator G that minimizes the loss function after the discriminator D has reached its optimal performance. The $\lambda 1$ and $\lambda 2$ are the weights of L1 and L2 losses, respectively. Trial-and-error model tuning experiments were conducted to determine the most suitable values for these weights, ensuring the best fit for the specific domain of tasks.

To further improve training and enhance model robustness, variability was introduced through data augmentation techniques applied to the input images instead of using an explicit noise vector. This approach effectively serves the same function as a noise distribution in the latent space of a vanilla GAN network to enhance the training process, considering that the oriented matter of columnar grains formed along a vertical direction of the printed block (building direction of the AM block); to better preserve the directionality of columnar grain morphology, the horizontal flip was applied to the original extracted microstructure images instead of using vertical flip or other orientation rotation techniques. Additionally, a median filter is applied to enhance the grain patterns while reducing the noise from low-resolution images. Moreover, color transformation was also considered in enhancing the variability of images, including color mapping conversion through the jet color map and gray transformation with fine enhancement on the boundary of grains. By introducing various image filters and augmentation techniques to target images, this work aims to improve the robustness and generalization of the model.

2.5 Evaluation metrics

To quantitatively evaluate the machine learning model, a novel measurement approach specifically tailored to meet the unique demands of microstructure prediction was developed. Instead of using conventional pixel-by-pixel evaluation methods commonly applied in semantic segmentation or object detection tasks in computer vision applications, a grain-size-based evaluation was designed to better capture the characteristics of the predicted grains. The goal is to measure the similarity between the predicted grain structures and the original microstructure images in terms of their morphology and size distribution. The proposed method consists of two steps. First, an algorithm to automatically segment the grains was developed. Second, the segmented grains were compared by analyzing the distribution of grain sizes and shapes using histogram-based similarity metrics. The algorithm for microstructure segmentation is illustrated in Fig. 7.

In the second step, the segmented results obtained from step one were utilized as input to compute the weighted average grain size for each image and perform statistical analysis to construct histograms. Subsequently, the histograms derived from the original (KMC simulated ground truth) microstructure images with those from the ML predicted ones were compared. To ensure a comprehensive evaluation instead of relying solely on one metric, both similarity and distance scores were calculated. The similarity score is calculated based on the intersection of two histograms, providing a measure of their overlapping area. Conversely, the distance score is determined using the Bhattacharyya method [47], which quantifies the divergence between the two histograms. A higher similarity score suggests a closer resemblance between the two histograms, whereas a smaller distance score is expected due to its reflection of the dissimilarity between the compared images. The calculation of both similarity and distance scores can be defined as shown in Eqs. 11 and 12. To calculate the similarity score, as shown in Eq. 11, the histogram intersection method is adopted to measure the overlap between two histograms (H_1 and H_2). For each bin I, the minimum value between the two histograms

Algorithm 1 Microstructure Segmentation

Input:

Dataset T
Gaussian filter radius r_{gaussian}
Sobel edge detection threshold T_{sobel}
Number of dilation iterations n_{dilate}

Output:

Segmented microstructure images

for each input image I_i in the dataset T **do**
  Convert I_i to grayscale and store it as $I_{i,gray}$
  Apply Gaussian filter with radius r_{gaussian} to $I_{i,gray}$ and store the filtered image as $I_{i,filtered}$
  Apply Sobel edge detection with threshold T_{sobel} to $I_{i,filtered}$ and store the edge image as $I_{i,edges}$
  Binarize the edge image $I_{i,edges}$ and store the binarized image as $I_{i,binarized}$
  Perform segmentation using watershed algorithm on $I_{i,binarized}$ and obtain segmented regions
  for each segmented region R_j **do**
    Number the pixels of R_j and obtain a labeled region
  end for
  Combine all labeled regions and obtain a labeled image $I_{i,labeled}$
  Save or display segmented microstructure image $I_{i,labeled}$
end for

(a)

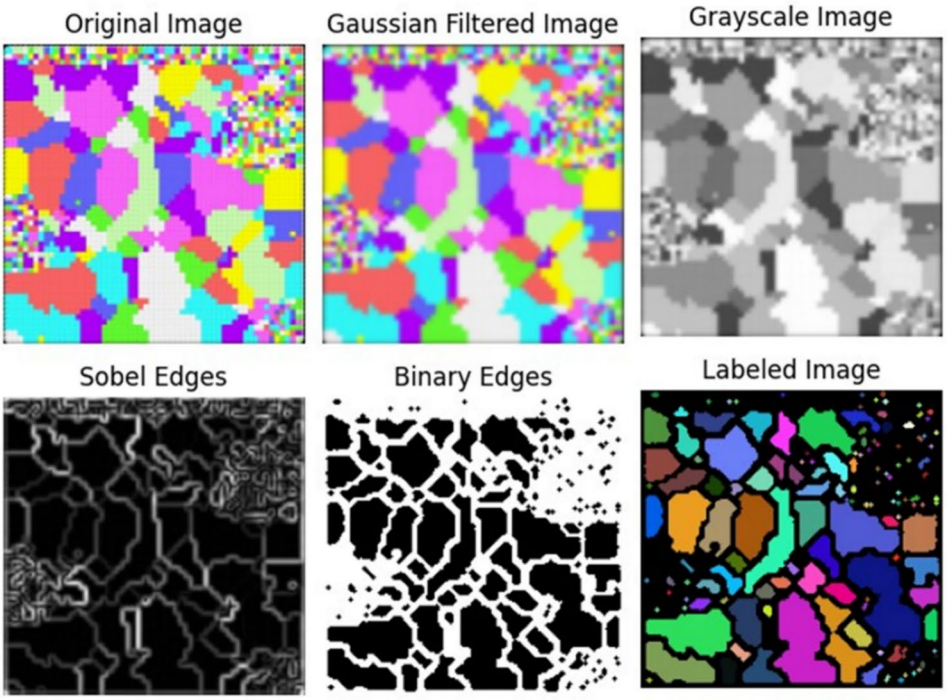

(b)

Fig. 7 **a** Algorithm for microstructure segmentation. **b** Sequential illustration of microstructure segmentation process for grain size estimation

is taken, representing the extent of overlap in that bin. The final similarity score is obtained by summing these minimum values across all bins. In addition, as shown in Eq. 12, N represents the number of bins in the histograms. To obtain the distance score, the sum of the products of the corresponding bin values from the histograms is first calculated. This sum is then divided by the square root of the product of the norms of the two histograms, multiplied by the square of the number of bins. This process ensures that the distance measure is scale-invariant.

$$s(H_1, H_2) = \sum_I \min\left(H_1(I), H_2(I)\right) \tag{11}$$

$$d(H_1, H_2) = \sqrt{1 - \frac{1}{\sqrt{|H_1||H_2|N^2}} \sum_I H_1(I) \cdot H_2(I)} \tag{12}$$

3 Prediction of microstructure

The Pix2Pix deep learning model was applied in this study to predict microstructural images from process parameters in additive manufacturing (AM). Given the uniqueness of this application, previously established hyperparameters for model training [48] were not directly applicable. Consequently, various hyperparameter configurations were explored for training, including (λ_1, λ_2, $\mathcal{L}_{\text{cGAN}}$) (Eqs. 8–10), building upon prior research [48, 49]. The total generator loss, consisting of a weighted sum of three individual losses (L1, L2, and GAN) as defined in Eqs. 8–10, was optimized by testing different weight combinations to identify the most suitable configuration for accurate microstructure predictions in AM. The configurations tested included (1) GAN-100, with data augmentation, which involved a 100% contribution from GAN loss (full adversarial training); (2) GAN-100, without data augmentation; and (3) combinations of L1 and L2 with a minimal contribution. The results indicated that increasing the contribution from L1 and L2 led to reduced model performance compared to models relying solely on GAN loss.

As demonstrated in Fig. 8, the model trained with full adversarial training (GAN-100) exhibited the best performance in terms of the visual similarity of generated microstructures to ground truth images. This finding contrasts with the author's earlier studies [48, 49], where assigning greater weight to L2 loss was advantageous. In the current study, however, such an increase in L2 loss weightage resulted in spurious microstructural features lacking physical validity, as illustrated in Fig. 8. Additionally, data augmentation, in conjunction with pure GAN loss (GAN-100), generally improved model performance. The model trained without augmentation displayed lower similarity to the ground truth, as evidenced by a higher Bhattacharyya distance score (0.253) compared to the augmented model (0.239).

Unlike many previous studies, where the Pix2Pix framework was effectively utilized for tasks such as image denoising, style transfer, and super-resolution [48, 49], the current task differed significantly due to the lack of spatial correlation between input and output domains. While conventional tasks typically exhibit high spatial correlation between input and output image features, the task of generating microstructures from "coded process parameter images" involved non-spatial correlations or mappings, as depicted in Fig. 5. As a result, hyperparameters that performed well in earlier works failed to produce satisfactory results in this case. Instead, it was observed that higher GAN weightage generated microstructures with features closely resembling ground truth. The assessment of microstructural correctness is often subjective and closely tied to human perception. Previous studies have shown that GAN loss is particularly effective in scenarios where the perceptual similarity between the machine learning output and ground truth is prioritized over exact pixel-by-pixel correspondence. The improved performance observed with higher GAN loss contributions aligned with previous findings, where feedback from the discriminator in the training loop enhanced outcomes. This justified the choice of employing GAN-based deep learning for the present study.

Key features in this task included grains with uniform color values within their interiors and grain boundaries with characteristic dihedral angles typical of recrystallized and columnar microstructures. Nucleated or recrystallized

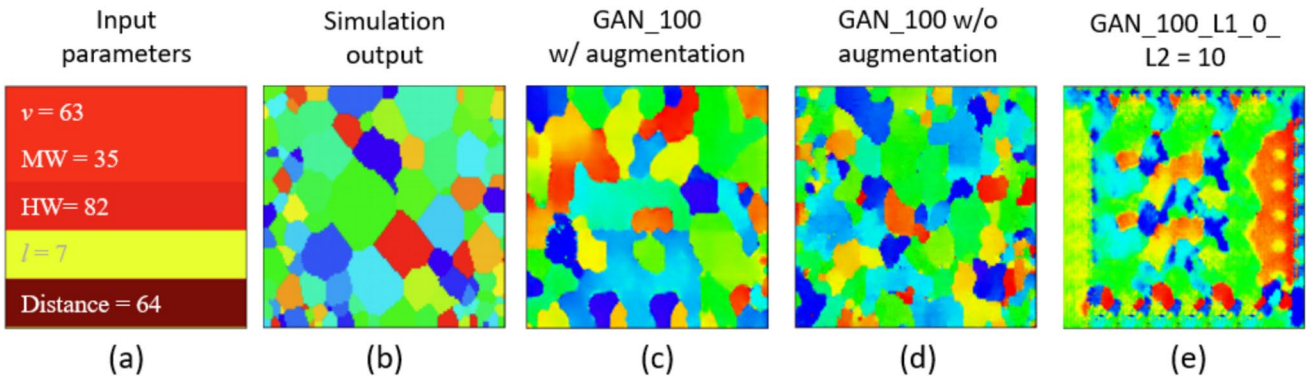

Fig. 8 Comparison of ML output with different settings of loss functions. **a** Coded map of input parameters (speed = 63, melt pool width = 35, HAZ width = 82, layer thickness = 7, xy-plane distance = 64); **b** ground truth; **c** GAN-100; **d** GAN-100 without augmentation; **e** GAN 100 and L2-10

grains from the heat-affected zone (HAZ) were expected to exhibit minimal intra-grain misorientation due to the formation of strain-free grains during solidification and subsequent growth during reheat cycles, characteristic of multi-track and multi-layer AM processes. This manifested as uniform color across pixels within the same grain, as experimentally observed through techniques like electron backscatter diffraction [49]. In contrast, deformed materials typically exhibited significant intra-grain color gradients. The ground truth microstructures generated through Kinetic Monte Carlo (KMC) simulations incorporated this information by assigning identical spins (rendered as identical colors in OVITO for visualization) to lattice points within the same grain. Grain boundaries typical of AM microstructures were characterized by dihedral angles of 120° at tri-junctions of grain boundaries, particularly in equiaxed grains. KMC simulations ensured these microstructural features through grain boundary mobility laws, generating grain boundaries with curvatures satisfying these laws and forming dihedral angles at tri-junctions, capturing the physics of grain nucleation and growth.

The machine learning model, lacking explicit encoding of such physical laws, was expected to learn these microstructural evolution dynamics through the mapping of input process parameters to output domains. This required a diverse dataset, necessitating a large number of training images. The dataset in this study, comprising data from over 1500 KMC simulations, addressed this issue to a considerable extent, though further improvements were anticipated with increased input data volume and diversity. The close alignment of GAN-based machine learning predictions, as shown in Fig. 8, with expected microstructural grain morphologies was evaluated within this context. Given the observed superiority of the GAN-based model, all machine learning predictions throughout the manuscript were generated using the model trained with 100% GAN loss contribution. Microstructure prediction performance of the current ML approach is summarized in Fig. 9 which shows results from various parameter selections on the test data set (process parameter combinations). It can be observed that the model is able to capture the trend of decreasing grain size with scanning speeds (one of the crucial process parameters), in line with the corresponding ground truth KMC results. As the scanning speed increased, the grain size of the predicted microstructures decreased. Although grain size variation as a function of laser scanning speed was captured

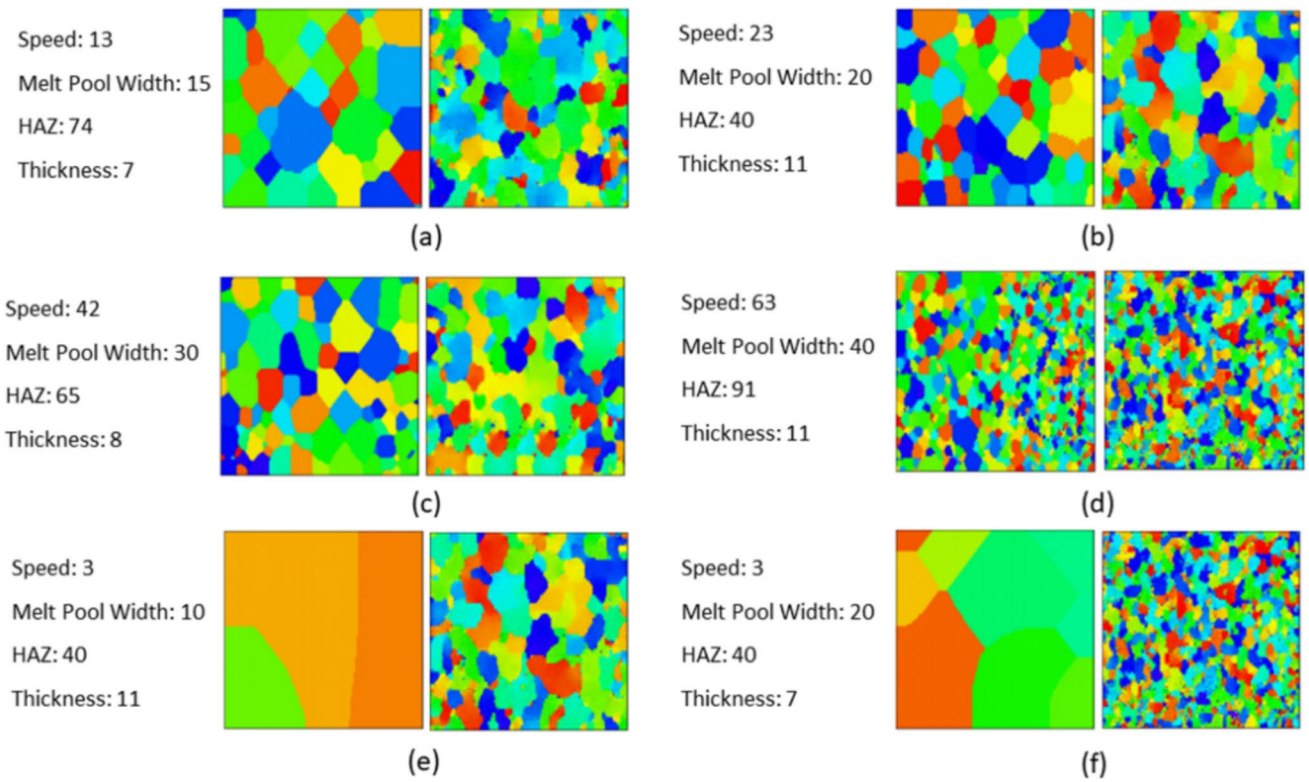

Fig. 9 Summary of ML microstructure prediction results along with corresponding input process parameters. For each case (from **a** to **f**), process conditions, KMC-generated ground truth, and corresponding ML output have been included. While the cases of **a** to **d** represented fairly good predictions of equiaxed grins, cases **e** and **f** indicate the failure of the model for accurate microstructure generation corresponding to the columnar grain case

well, the inference performance was observed to be inferior for cases corresponding to columnar grains in comparison to cases of equiaxed ones. The inference of smaller equiaxed grains outperformed (as they corresponded correctly in terms of visual similarity and size distribution to respective ground truth KMC simulated microstructures) that of larger grains. This could be likely due to bias in the training dataset, which contains a higher proportion of smaller equiaxed grains from the data collection process corresponding to the applied range of parameters employed in the current work.

Despite this observed limitation in predicting the process parameter regime associated with columnar grains, the current study largely demonstrates the feasibility of realistic microstructure prediction for complex additive manufacturing processes. This lays the groundwork for future research to address data imbalance issues and improve predictions for columnar grain cases as well.

While visual comparisons of machine learning (ML) results with corresponding ground truth images are informative, it is often preferable to quantify the model's

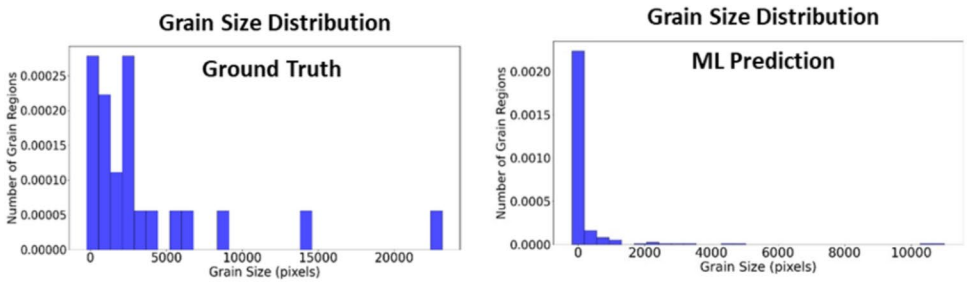

(a) Speed = 13, MP Width = 15, HAZ Width = 74, Layer thickness = 7

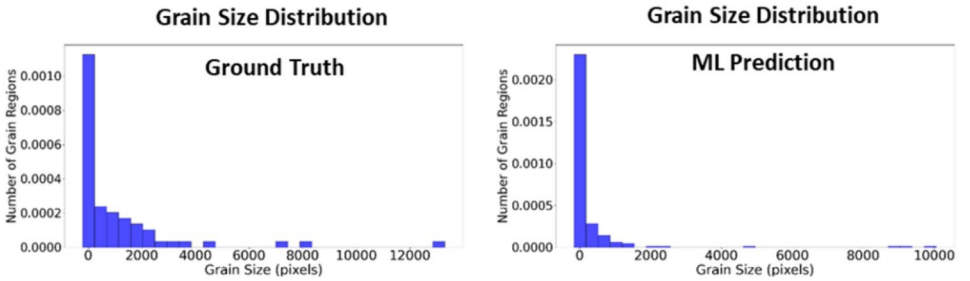

(b) Speed = 42, MP Width = 30, HAZ Width = 65, Layer thickness = 8

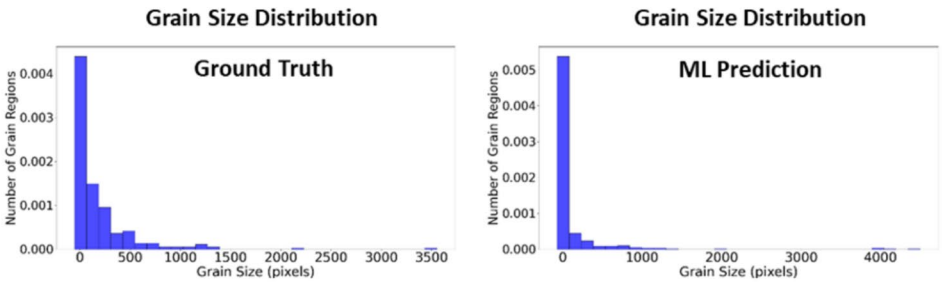

(c) Speed = 52, MP Width = 10, HAZ Width = 40, Layer thickness = 11

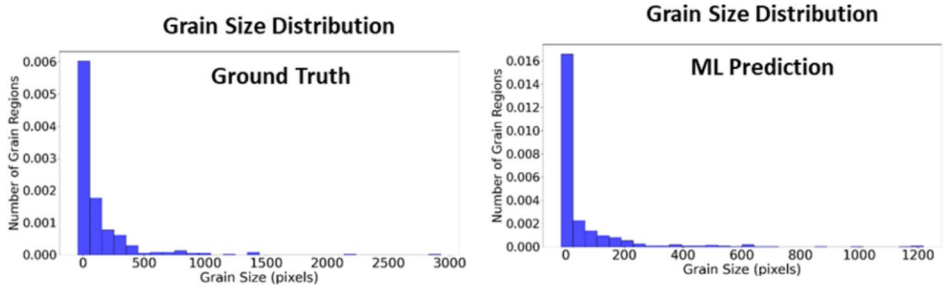

(d) Speed = 63, MP Width = 30, HAZ Width = 40, Layer thickness = 7

Fig. 10 Machine learning predicted results—grain size distribution. **a**–**d** Different examples from the test data set

performance through quantitative comparisons with reference to ground truth microstructures. Metrics such as SSIM and MSE are typically employed for such comparisons. However, in this case, these popular metrics were not applicable, as the features of interest—grain morphology (equiaxed vs. columnar) and grain size distribution—are not reflected by absolute color distributions or pixel color intensities. Pixel-level metrics such as MSE and SSIM fail to capture the higher-level features relevant to microstructural quantification. Therefore, to quantitatively assess the predicted results, grain size distributions were presented for various test cases in Fig. 10. The left side of the figure displayed statistical data from ground truth microstructures, while the right side illustrated the grain size distributions of the predicted results. The method effectively captured the grain size distribution, particularly for medium- and small-sized grains. For instance, case (Fig. 10d) achieved the highest similarity score of 3.88e–2 and the lowest distance of 0.29, while case (Fig. 10b) achieved a secondary similarity score of $0.75e-3$ and a distance score of 0.35.

Despite the impressive performance of the model in predicting fine equiaxed grain morphologies, it encountered difficulties in predicting columnar grains, as observed in the case of Fig. 10f. Larger grains were sometimes mispredicted as smaller grains, which could potentially be mitigated by introducing a more balanced dataset with a higher proportion of large and columnar-shaped grains. Overall, the predictive models demonstrated a strong capability to predict microstructures across varying process parameters and accurately capture grain features, marking a significant achievement in the literature.

4 Conclusions

The study successfully demonstrated the effectiveness of advanced machine learning and deep learning techniques, particularly through the use of conditional generative adversarial networks (cGANs), in predicting microstructural variations from process parameters in additive manufacturing. This approach effectively bridges the gap between theoretical simulations and practical applications, enhancing the predictive accuracy of microstructural characteristics. The key achievements of our research are summarized as follows:

- A comprehensive new database of Kinetic Monte Carlo-based simulations has been introduced, spanning a range of process parameters and grain morphologies. This resource can significantly benefit future ML research into the analysis of microstructures relative to process parameters.
- The model achieved the highest similarity score of $3.88e-2$ and the lowest distance score of 0.29, reflecting its efficacy in reproducing the ground truth microstructures.
- Challenges were observed in predicting columnar grains, suggesting that a more balanced dataset with a higher proportion of larger and columnar grains could improve accuracy.

Author contribution All authors contributed to the study's conception and design. Zhaochen Gu, Aishwarya Manjunath, A. Anantatamukala, and K.V. Mani Krishna performed ML modeling, data collection, and analysis. Shashank Sharma, K.V. Mani Krishna, and Zhaochen Gu wrote the first draft of the manuscript. All authors commented on previous versions of the manuscript. Narendra B. Dahotre and Song. Fu edited and corrected the manuscript. All authors read and approved the final manuscript.

Funding Authors acknowledge the support of Center for Agile and Adaptive Additive Manufacturing (CAAAM) funded through State of Texas Appropriation: 190405-105-805008-220 during preparation of this manuscript and Material Research Facility (MRF) for access to microscopy at the University of North Texas.

Data availability The data generated in this study are available from the corresponding authors upon reasonable request.

Declarations

Competing interests The authors declare no competing interests.

References

1. Dahotre NB, Pantawane MV, Sharma S (2022) Laser-based additive manufacturing: modeling, simulation, and experiments, first. Wiley, Berlin
2. Sharma S, Joshi SS, Pantawane MV et al (2023) Multiphysics multi-scale computational framework for linking process–structure–property relationships in metal additive manufacturing: a critical review. Int Mater Rev 68:943–1009. https://doi.org/10.1080/09506608.2023.2169501
3. Gatsos T, Elsayed KA, Zhai Y, Lados DA (2020) Review on computational modeling of process–microstructure–property relationships in metal additive manufacturing. Jom 72:403–419. https://doi.org/10.1007/s11837-019-03913-x
4. Durga A, Lindwall G (2023) Modelling columnar-to-equiaxed transition during fusion-based metal additive manufacturing 2023:2214–8604. https://doi.org/10.1016/j.addma.2023.103802
5. Tan JHK, Sing SL, Yeong WY (2020) Microstructure modelling for metallic additive manufacturing: a review. Virtual Phys Prototyp 15:87–105. https://doi.org/10.1080/17452759.2019.1677345
6. Liu P, Wang Z, Xiao Y et al (2019). Insight into the mechanisms of columnar to equiaxed grain transition during metallic additive manufacturing. https://doi.org/10.1016/j.addma.2018.12.019
7. Gatsos T, Elsayed KA, Zhai Y, Lados DA (2020) Review on computational modeling of process–microstructure–property relationships in metal additive manufacturing. JOM 72:403–419. https://doi.org/10.1007/S11837--X/TABLES/2

8. Körner C, Markl M, Koepf JA (2020) Modeling and simulation of microstructure evolution for additive manufacturing of metals: a critical review. Metall Mater Trans A Phys Metall Mater Sci 51:4970–4983. https://doi.org/10.1007/S11661--3/FIGURES/8
9. Parsazadeh M, Sharma S, Dahotre N (2023) Towards the next generation of machine learning models in additive manufacturing: a review of process dependent material evolution. https://doi.org/10.1016/j.pmatsci.2023.101102
10. Tang J, Geng X, Li D et al (2021) Machine learning-based microstructure prediction during laser sintering of alumina. Sci Rep 11:1–10. https://doi.org/10.1038/s41598-021-89816-x
11. Herriott C, Spear AD (2020) Predicting microstructure-dependent mechanical properties in additively manufactured metals with machine- and deep-learning methods. Comput Mater Sci 175:109599. https://doi.org/10.1016/J.COMMATSCI.2020.109599
12. Gadelha M, Maji S, Wang R (2017) 3D shape induction from 2D views of multiple objects. In: 2017 International Conference on 3D Vision (3DV). IEEE, pp 402–411
13. Hsu T, Epting WK, Kim H et al (2021) Microstructure generation via generative adversarial network for heterogeneous, topologically complex 3D materials. JOM 73:90–102. https://doi.org/10.1007/s11837--y
14. Wu J, Zhang C, Xue T, et al (2016) Learning a probabilistic latent space of object shapes via 3D generative-adversarial modeling. In: Lee D, Sugiyama M, Luxburg U, et al (eds) Advances in Neural Information Processing Systems. Curran Associates, Inc
15. Allen-Zhu Z, Li Y (2021) Forward super-resolution: how can GANs learn hierarchical generative models for real-world distributions. arXiv ePrint
16. de Haan K, Ballard ZS, Rivenson Y et al (2019) Resolution enhancement in scanning electron microscopy using deep learning. Sci Rep 9:12050. https://doi.org/10.1038/s41598--2
17. Anantatamukala A, Krishna KVM, Dahotre NB (2023) Generative adversarial networks assisted machine learning based automated quantification of grain size from scanning electron microscope back scatter images. Mater Charact 206:113396. https://doi.org/10.1016/j.matchar.2023.113396
18. Tripathi S, Lipton ZC, Nguyen TQ (2018) Correction by projection: denoising images with generative adversarial networks.arXiv preprint arXiv:1803.04477. https://doi.org/10.48550/arXiv.1803.04477
19. Wang F, Henninen TR, Keller D, Erni R (2020) Noise2Atom: unsupervised denoising for scanning transmission electron microscopy images. Appl Microsc 50:23. https://doi.org/10.1186/s42649--8
20. Cang R, Li H, Yao H et al (2018) Improving direct physical properties prediction of heterogeneous materials from imaging data via convolutional neural network and a morphology-aware generative model. Comput Mater Sci 150:212–221. https://doi.org/10.1016/j.commatsci.2018.03.074
21. Chung J, Shen B, Kong ZJ (2024) Anomaly detection in additive manufacturing processes using supervised classification with imbalanced sensor data based on generative adversarial network. J Intell Manuf 35:2387–2406. https://doi.org/10.1007/S10845--8/TABLES/12
22. Tang J (2021) Deep learning-guided prediction of material's microstructures and applications to advanced manufacturing. All Dissertations
23. Pütz F, Henrich M, Fehlemann N (2020) Generating input data for microstructure modelling: a deep learning approach using generative adversarial networks. Materials 13:4236. https://doi.org/10.3390/MA13194236
24. Wang C, Chandra S, Huang S et al (2023) Unraveling process-microstructure-property correlations in powder-bed fusion additive manufacturing through information-rich surface features with deep learning. J Mater Process Technol 311:117804. https://doi.org/10.1016/J.JMATPROTEC.2022.117804
25. Ramlatchan A, Li Y, Zubair M et al (2022) Evaluation of generative models for predicting microstructure geometries in laser powder bed fusion additive manufacturing (Doctoral dissertation, Old Dominion University)
26. Rodgers TM, Madison JD, Tikare V (2017) Simulation of metal additive manufacturing microstructures using Kinetic Monte Carlo. Comput Mater Sci 135:78–89. https://doi.org/10.1016/J.COMMATSCI.2017.03.053
27. Rodgers TM, Moser D, Abdeljawad F et al (2021) Simulation of powder bed metal additive manufacturing microstructures with coupled finite difference-Monte Carlo method. Addit Manuf 41:101953. https://doi.org/10.1016/J.ADDMA.2021.101953
28. SPPARKS Kinetic and Metropolis Monte Carlo simulator. https://github.com/spparks/spparks. Accessed 2 Jul 2024
29. Isola P, Zhu J-Y, Zhou T, Efros AA (2017) Image-to-image translation with conditional adversarial networks. In: 2017 IEEE Conference on Computer Vision and Pattern Recognition (CVPR). IEEE, pp 5967–5976
30. Kurz W, Trivedi R (1994) Rapid solidification processing and microstructure formation. Mater Sci Eng, A 179–180:46–51. https://doi.org/10.1016/(94)
31. Davis AE, Wainwright J, Sahu VK et al (2024) Achieving a columnar-to-equiaxed transition through dendrite twinning in high deposition rate additively manufactured titanium alloys. Metall and Mater Trans A 55:1765–1787. https://doi.org/10.1007/s11661--7
32. Gäumann M, Bezençon C, Canalis P, Kurz W (2001) Single-crystal laser deposition of superalloys: processing–microstructure maps. Acta Mater 49:1051–1062. https://doi.org/10.1016/S1359-6454(00)
33. Singh AK, Mundada Y, Bajaj P, et al (2023) Microstructure engineering during directed energy deposition of Al-0.5Sc-0.5Si using heated build platform. Int J Heat Mass Transf 202:123679. https://doi.org/10.1016/j.ijheatmasstransfer.2022.123679
34. Gao N, Liu XW, Yin ZH et al (2024) Design solutes to achieve columnar-to-equiaxed transition and grain refinement in cast multi-principal-element alloys. Metall Mater Trans A Phys Metall Mater Sci 55:1397–1408. https://doi.org/10.1007/S11661--9/FIGURES/10
35. Guan S, Solberg K, Wan D, et al (2019) Formation of fully equiaxed grain microstructure in additively manufactured AlCoCrFeNiTi0.5 high entropy alloy. Mater Des 184:108202. https://doi.org/10.1016/J.MATDES.2019.108202
36. Martorano MA, Biscuola VB (2009) Predicting the columnar-to-equiaxed transition for a distribution of nucleation undercoolings. Acta Mater 57:607–615. https://doi.org/10.1016/J.ACTAMAT.2008.10.001
37. Seredyński M, Rebow M, Banaszek J (2018) The role of the dendritic growth model dimensionality in predicting the columnar to equiaxed transition (CET). Heat Mass Tran/Waerme-und Stoffuebertragung 54:2581–2588. https://doi.org/10.1007/S00231--Z/FIGURES/9
38. Rodgers TM, Madison JD, Tikare V, Maguire MC (2016) Predicting mesoscale microstructural evolution in electron beam welding. JOM 68:1419–1426. https://doi.org/10.1007/S11837--8/FIGURES/7
39. Mitchell JA, Abdeljawad F, Battaile C et al (2023) Parallel simulation via SPPARKS of on-lattice kinetic and Metropolis Monte Carlo models for materials processing. Model Simul Mat Sci Eng 31:55001. https://doi.org/10.1088/1361-651X/accc4b
40. Texas Advanced Computing Center (TACC). http://www.tacc.utexas.edu. Accessed 2 Jul 2024

41. Stukowski A (2010) Visualization and analysis of atomistic simulation data with OVITO–the open visualization tool. Model Simul Mat Sci Eng 18:015012. https://doi.org/10.1088/0965-0393/18/1/015012
42. Ronneberger O, Fischer P, Brox T (2015) U-net: Convolutional networks for biomedical image segmentation. In Medical image computing and computer-assisted intervention–MICCAI 2015: 18th International Conference, Proceedings, Part III vol 18. Springer international publishing, Munich, pp 234–241
43. Ioffe S, Szegedy C (2015) Batch normalization: accelerating deep network training by reducing internal covariate shift. In: pmlr (ed) International conference on machine learning, pp 448–456
44. Agarap AF (2018) Deep learning using rectified linear units (ReLU). arXiv preprint arXiv:1803.08375. https://doi.org/10.48550/arXiv.1803.08375
45. Kingma DP, Ba J (2014) Adam: A method for stochastic optimization. arXiv preprint arXiv:1412.6980. https://doi.org/10.48550/arXiv.1412.6980
46. Mandt S, Hoffman MD, Blei DM (2017) Stochastic gradient descent as approximate Bayesian inference. J Mach Learn Res 18:4873–4907
47. Kailath T (1967) The divergence and Bhattacharyya distance measures in signal selection. IEEE Trans Commun 15:52–60. https://doi.org/10.1109/TCOM.1967.1089532
48. Anantatamukala A, Krishna KVM, Dahotre NB (2023) Generative adversarial networks assisted machine learning based automated quantification of grain size from scanning electron microscope back scatter images. Mater Charact 206. https://doi.org/10.1016/j.matchar.2023.113396
49. Krishna KVM, Madhavan R, Pantawane MV et al (2023) Machine learning based de-noising of electron back scatter patterns of various crystallographic metallic materials fabricated using laser directed energy deposition. Ultramicroscopy 247:113703. https://doi.org/10.1016/J.ULTRAMIC.2023.113703